Journal of Volcanology and Geothermal Research 370 (2019) 51–64

Contents lists available at ScienceDirect

Journal of Volcanology and Geothermal Research

journal homepage: www.elsevier.com/locate/jvolgeores

Morphologic variation of an evolving dome controlled by the extrusion of finite yield strength magma

Taha Husain [a,*], Derek Elsworth [a], Barry Voight [b], Glen Mattioli [c], Pamela Jansma [d]

[a] Energy and Mineral Engineering, G3 Center and EMS Energy Institute, The Pennsylvania State University, University Park, PA 16802, United States of America
[b] Geosciences, The Pennsylvania State University, University Park, PA 16802, United States of America
[c] Director of Geodetic Infrastructure, Geodetic Infrastructure, UNAVCO, Boulder, CO 80301, United States of America
[d] Dean, College of Liberal Arts and Sciences, University of Colorado, Denver, CO 80217, United States of America

ARTICLE INFO

Article history:
Received 30 May 2018
Received in revised form 22 December 2018
Accepted 4 January 2019
Available online 08 January 2019

ABSTRACT

Degassing-induced crystallization in volatile rich intermediate composition magmas results in material stiffening and strengthening that prior to solidification is reflected in non-Newtonian rheology. We explore the effects of a spectrum of such rheological regimes on eruptive style and morphologic evolution of lava domes, using a two-dimensional (2D) particle-dynamics model for a spreading viscoplastic (Bingham) fluid. We assume that the ductile magma core of a 2D synthetic lava dome develops finite yield strength, and that deformable frictional talus evolves from a carapace that caps the magma core. Our new model is calibrated against an existing analytical model for a spreading viscoplastic lava dome and is further compared against observational data of lava dome growth. Results indicate that a degassing-induced increase in strength of the injected magma causes a transition in the lava dome morphology from a dome with low surface relief evolving endogenously (with apparent bulk yield strength - $10^4 < \tau_{0_a} < 10^6$ Pa), to a Pelean lava dome with spines ($\tau_{0_a} > 10^5 - 10^6$ Pa) extruded through the dome carapace. The virtual lava dome with $\tau_{0_a} = 0.6$ MPa shows good agreement with the observed dome heights observed at the Soufriere Hills Volcano, Montserrat during a period of endogenous growth. The calculated apparent flow viscosity (1.36×10^{11} Pa·s for $\tau_{0_a} = 0.6$ MPa) is in the range of estimated viscosities (10^9 to 10^{12} Pa·s) for andesitic-dacitic crystal-rich lavas. Our model results indicate a strong correlation between apparent yield strength and dome morphology, with both controlled by degassing-induced crystallization and extrusion rate.

Published by Elsevier B.V.

1. Introduction

Magma rheology is affected by pressure, temperature, volatile content, and crystallization, with these parameters varying throughout the magmatic plumbing systems with a strong feedback on dome evolution (Stasiuk and Jaupart, 1997). Changes in magma rheology are manifested in effusion rate and lava dome morphology. Observations at such volcanoes as Merapi in Java, and Soufriere Hills Volcano on Montserrat, indicate changes in effusion rate and rheology that are directly reflected in transitions between exogenous to endogenous growth styles (Hale and Wadge, 2008; Voight et al., 2000; Watts et al., 2002).

Degassing-induced crystallization is the dominant process of stiffening in intermediate-composition magmas, such as at Soufrière Hills Volcano (Sparks, 1997; Sparks et al., 2000) and at Merapi (Hammer and Rutherford, 2002; Innocenti et al., 2013a, 2013b), although cooling may also play a role. Volatile exsolution from magma triggers crystallization of microlites that results in rheological stiffening. The extent of rheological stiffening controls the gain in mechanical strength, which in turn affects flow patterns within a lava dome (Lavallée et al., 2007). Degassed magma forms highly-crystallined lava that may evolve into spines, while magma remaining rich in volatiles is more ductile and this promotes low-amplitude domes and lava lobes.

Different growth patterns are observed for varying rates of surface cooling, degassing, and magma extrusion (Fink and Griffiths, 1990; Watts et al., 2002). Previous models of lava dome morphology considered a rigid outer shell (Hale and Wadge, 2003; Iverson, 1990), and growth controlled by internal magma yield strength (Blake, 1990). Non-Newtonian behavior of the magma (including yield strength) affects flow geometry and thus observed lava dome morphology can be a proxy for extrusion rate (Tallarico and Dragoni, 2000; Watts et al., 2002). At low extrusion rates (less than ~ 1 m^3/s) highly crystalline magma (85% to 95% solid fraction) at Soufriere Hills Volcano, Montserrat, is observed to predominantly extrude exogenously and to produce spines (Sparks et al., 2000). Both scale models and continuum mechanical models have improved our understanding of domes (Blake, 1990; Fink and Griffiths, 1990). More recently, dynamic discrete element (particle) models have been used to follow gravitational deformations of

* Corresponding author.
E-mail address: tahamurtuzahusain@gmail.com (T. Husain).

https://doi.org/10.1016/j.jvolgeores.2019.01.010
0377-0273/Published by Elsevier B.V.

aggregates of granular particles that evolve self-similarly (Morgan and McGovern, 2005a, 2005b), and this approach is used to study lava dome morphologies that reflect rheological stiffening (Husain et al., 2014).

Here we extend the latter approach to further develop a 2D model to represent growth of a lava dome above a horizontal foundation, where the dome grows about the axis of a vertical conduit. The 2D model only considers two force components (neglecting the out-of-plane component for calculations using the equation of motion and the force-displacement laws) and a moment component, unlike the case of a 3D model (three components each of force and moment). The model uses the discrete element method (DEM) (Cundall and Strack, 1979) in the particle-mechanics model to represent the injection of magma into a ductile dome core; on the dome exterior a brittle carapace of talus is developed (Husain et al., 2018, 2014, 2013). This model is used to examine the evolution of a synthetic dome, and further to decipher its resulting internal and external structure. The model illustrates the mechanics of the transition from endogenous to exogenous dome growth.

A magma flux with assumed composition and initial volatile content at depth, is specified as inputs to the system. The development of the dome morphology in the model is influenced by rate of magma influx, system-generated variations in magma viscosity and yield strength and frictional strength of the talus. In Section 3.1 we investigate the effect of magma yield strength on lava dome morphology and the transition from endogenous to exogenous styles of growth. In Section 3.2 we compare the results of the numerical simulations for an endogenously evolving lava dome with an analytical model and laboratory observations of a spreading viscoplastic material on a rigid horizontal surface (Blake, 1990; Griffiths and Fink, 1997). The model is then extended to the lava dome growth observed at SHV, Montserrat for the period of October 1996, during which time the dome grew endogenously.

2. Model description

We represent the lava dome as an aggregate of discrete particles representing "packets of magma" (Cundall and Strack, 1979). The application of discrete element methods (DEM) in physics and fluid mechanics is well established (Allen and Tildesley, 1989; Matuttis and Chen, 2014). Our model incorporates granular contact mechanics and maps the stress distribution in a deforming aggregate. The model accommodates local deformation in an idealized carapace that is analogous to displacement on fractures or boundaries of blocks, distributed heterogenously through the structure. The code uses a"soft particle dynamics" mode (Cundall and Strack, 1979) to include elastic particle deformation at contacts; interparticle contact laws play an important role in defining the behavior of the assemblage (Morgan and McGovern, 2005a, 2005b).

The synthetic 2D lava dome grows over a rigid horizontal base fed by a vertical conduit with a specified flow-rate history. Particles of specified diameter (1.5 m diameter (D) in this study) are idealized as "packets of magma" that reflect bulk magma behavior for computational modeling purposes. The ascending magma is treated as bubble free with a constant density ρ (Stasiuk et al., 1993). Studies show that magma with crystal content lower than 40% behaves as a Newtonian fluid for natural deformation rates (10^{-3} to 10^{-7} s^{-1}) (Caricchi et al., 2007; Lejeune and Richet, 1995; Pinkerton and Stevenson, 1992), while a further increase in the crystal content generates a strength component that is reflected in the non-Newtonian behavior of the magma (Blake, 1990; Lavallée et al., 2007; Melnik and Sparks, 2005; Voight et al., 2002). The magma flow (velocity profile) is assumed fully developed for high viscosity fluids in the conduit with a very small width-to-length ratio (Stasiuk and Jaupart, 1997). Magma flow during an eruptive cycle is in the laminar regime and follows Poiseuille's law (de' Michieli Vitturi et al., 2008; Huppert et al., 1982; Melnik, 2000; Melnik and Sparks, 2005; Stevenson and Blake, 1998). The equivalent flow velocity (v_{3D}^{avg} v_{3D}^{avg}) of the magma packets is given as,

$$v_{3D}^{avg} = {}^{Q_{3D}}/_{\pi r^2}\, v_{3D}^{avg} = {}^{Q_{3D}}/_{\pi r^2} \tag{1}$$

where the area of the conduit of radius r is $a_{3D} = \pi r^2 a_{3D} = \pi r^2$ for a representative 3D flow rate of $Q_{3D}Q_{3D}$. The flow velocity in the simulation runs is arbitrarily assumed (unless explicitly defined) to illustrate certain rheological effects that the model can represent. The flow velocity in 2D is specified as equal to the 3D velocity given by Eq. (1). The cross-sectional areas in 2D and 3D geometry are maintained equal and the representative characteristic width ($w_C w_C$) of the conduit in 2D for all model runs is as given in the Appendix A. Dimensions of the conduit are given in Table 1, and the basic geometry of the simulation is shown in Fig. 1.

Parallel bonds are used in our particulate mechanics model to represent the rheology of a crystal bearing magma with finite yield strength (Fig. 2). The total shear force ($F_t^s F_t^s$) in PFC^{2D} at time t after time step $\Delta\Delta t$ is associated with the parallel contact bond and is given by Eq. (2),

$$F_t^s = F_{t-\Delta t}^s + \Delta F_{\Delta t}^s \, F_t^s = F_{t-\Delta t}^s + \Delta F_{\Delta t}^s \tag{2}$$

where $\Delta F_{\Delta t}^s \Delta F_{\Delta t}^s$ is the incremental shear force generated over the timestep $\Delta\Delta\Delta t$. A parallel bond approximates the physical behavior of two bonded particles where torsion of the assemblage is resisted (as represented in Fig. 2a) (Delenne et al., 2004; Guo and Morgan, 2006; Itasca Consulting Group, 2004). The parallel bond is broken when the applied shear force ($F_{t-\Delta t}^s$) is equal to or exceeds the maximum shear stress (τ_{max}). Maximum shear stress (τ_{max}) for failure of the parallel bond is given as,

$$\tau_{max} = {}^{|F_{t-\Delta t}^s|}\Big/_{A} \tag{3}$$

$$\Delta\tau = {}^{\Delta F_{\Delta t}^s}\Big/_{A} = -k^s \Delta U^s \tag{4}$$

where $F_{t-\Delta t}^s$ is the shear loading for an area A and is given by Eq. (3). Eq. (4) represents the incremental shear stress ($\Delta\tau$) over a timestep Δt for a shear displacement of $\Delta U^s = V_i \Delta t$ after maximum shear stress (τ_{max}) is exceeded at (t -Δt). The parallel bond shear stiffness (k^s) is related to the plastic viscosity (η) as,

$$k^s = \frac{\eta}{\Delta t L_0} \tag{5}$$

where L_o is the original sample size (twice the particle diameter in this study) and V_i is the shear velocity (see Appendix A). Using Eq. (4) the plastic viscosity is correlated with the parallel bond shear stiffness in Eq. (5) (see Appendix A). The parallel bond is regenerated for a viscous fluid (represented by red particles in Fig. 1 and flow re-initiates upon the application of stress in excess of the yield stress.

Modes of deformation are influenced by mechanical properties of the particle assemblage (Morgan and McGovern, 2005b). Material stiffness depends on the composition of the magma, with combined effects of melt, crystal and volatiles. The formation of crystals and gas bubbles during magma ascent significantly alters the material properties of the flow and this in turn affects the morphology of the lava dome (Cashman and Blundy, 2000; Griffiths, 2000; Rust and Manga, 2002). As discussed above, there are two mechanisms that cause solidification of magma or lava: 1) cooling, particularly of an extruded lava surface, that stiffens the material and ultimately creates a solid exterior crust (Fink and Griffiths, 1990; Iverson, 1990); and 2) gas exsolution during magma ascent that increases magma liquidus temperature and promotes crystallization and ultimately solidification (Blundy et al., 2006; Blundy and Cashman, 2001; Cashman and Blundy, 2000; Couch et al., 2003; Hort, 1998). The brittle exterior carapace of a lava dome can present a significant obstacle to magma extrusion (Bourgouin et al., 2007),

Table 1
PFC model dimensions.

Conduit length (2D)	Equivalent conduit radius (3D)	Conduit characteristic width (2D)	Depth of conduit (2D)	Expanse of the base
30 m	15 m	23.6 m	750 m	1400 m

particularly for a carapace thickness > 10 m (Denlinger, 1990). The thermal conductivity of magma and wallrock, however, is very low and degassing-induced crystallization is the dominant mechanism for stiffening and solidification of intermediate composition magma (andesite and dacite) (Couch et al., 2003; Sparks et al., 2000; Clarke et al., 2007). The extent of crystallization is controlled by the mass of gas exsolved and is governed by Henry's law. Experiments to observe crystallization of plagioclase feldspar (Couch et al., 2003; Melnik and Sparks, 2005), which is the major crystallizing phase during decompression of andesitic magmas, provides an empirical correlation between liquidus/solidus temperature ($T_{liq,sol}$) as

$$T_{liq,sol} = a_T + b_T \ln(p) + c_T \ln(p)^2 + d_T \ln(p)^3 \quad (6)$$

and controlled by pressure p and empirical constants a_T, b_T, c_T and d_T. A least-squares best fit to the experimental data, defined by Eq. (6), yields the values of the constants (a_T, b_T, c_T and d_T) given in Table 2, which differ for liquid and solid states, depending on the extent of crystallization. Lava solidification is related to pressure using the solidus temperature ($T_{solidus}$) given by Eq. (6). The solidus temperature of a dynamic magmatic system can vary during its eruptive history. In our current model the solidus temperature is assumed constant. Experiments performed on lavas from Soufrière Hills volcano are used to constrain the variables that include pressure, temperature and water content; the solidus temperatures for SHV magmas range from 830 °C to 940 °C (Barclay et al., 1998; Rutherford and Devine, 2003) with solidus pressures between 0.1 and 5 MPa as Fig. 3 (Hale, 2008). Matrix glass composition tracks ground-mass crystallinity, which is used to obtain the pressure at which glass and crystal equilibrated (Blundy and Cashman, 2001). The composition can be used to obtain effective pressure at which the crystal growth kinetics are inhibited and the melt chemistry does not change further – the *closure pressure*. The closure pressure is controlled by the time available and kinetics of crystal nucleation and growth (Cashman and Blundy, 2000). Magma rheology depends strongly on the location and time the melt requires to attain the closure pressure (Hort, 1998). Studies suggest a sharp rheological change at a critical crystal fraction beyond which the solidified highly crystalline lava develops strong non-Newtonian properties and mechanical strength (Lavallée et al., 2007; Lejeune and Richet, 1995; Marsh, 1989; Melnik and Sparks, 2002).

In our models the transition of a soft dome core (indicated by red particles in Fig. 1) from a liquid mush to a solid carapace (that for simplicity we assume spontaneously breaks into talus, represented by yellow particles in Fig. 4) is defined by the solidus/closure pressure (Simmons et al., 2005). Magma undercooling promotes crystallization as the liquidus temperature increases while the magma pressure approaches the solidus/closure pressure (Fig. 3). We assume the magma is converted into a solid at the solidus/closure pressure. In our model the maximum principal stress exerted on each discrete particle is calculated, and if equal to or below the solidus pressure, the material properties of that particle are changed to match the values of a crystallized solid (talus). The transition from core (cohesion dominated – red particles in our figures) to talus (friction dominated – yellow particles) is a binary step-change in properties and is unidirectional – a subsequent increase in pressure will *not* enable a transition back to a liquid state. Comparison of the maximum principal stress for each particle at every time step helps update material properties, while identifying and tracking the core-talus interface.

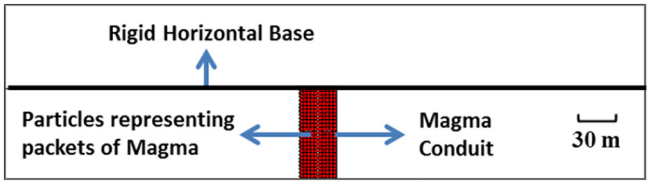

Fig. 1. Basic model setup in PFC^{2D} which includes the conduit (30 m wide opening with rigid walls) where the lava dome develops on a rigid horizontal surface (700 m long on either side of the conduit) and the red particles of 1.5 m radius represent magma that forms the volatile rich magma that forms the core in the lava dome. (For interpretation of the references to color in this figure legend, the reader is referred to the web version of this article.)

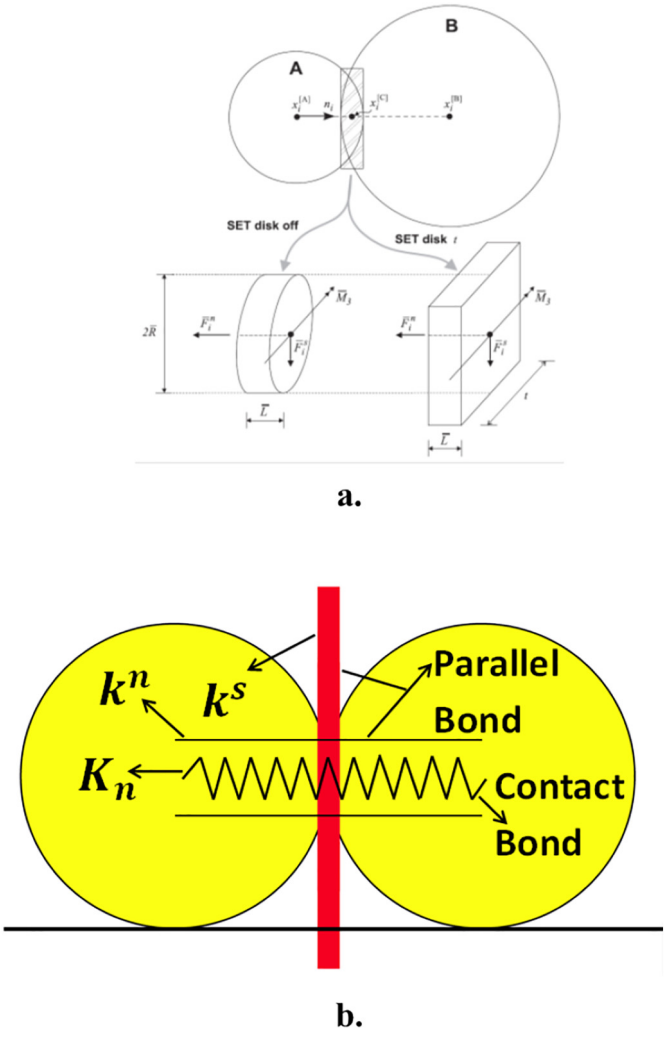

Fig. 2. a) Parallel bond depicted as a finite-sized piece of cementatious material (Itasca Consulting Group, 2004). b) Location of the linear contact bond and parallel bond in the PFC2D code (Husain et al., 2014).

Table 2
Constant for the empirical expression obtained for the phase behavior of magma (Melnik and Sparks, 2005).

Constant	Liquidus	Solidus
a_T	1465.5	1252.2
b_T	−31.4	−25.3
c_T	−2.8	−11.9
d_T	−0.41	1.17

The particle interaction for the talus are governed by the constitutive linear contact model, and the repulsive contact force in the normal and shear direction are given as,

$$F_n = k_n \delta_n \tag{7}$$

$$F_s = k_s \delta_s \tag{8}$$

where k_n and k_s are the contact stiffnesses in the normal and shear direction, with particle overlap in the respective directions represented by δ_n and δ_s in Eqs. (7), (8). The macroscopic material stiffness (Young's modulus E and Shear Modulus G) of the particle arrangement given in Fig. 2 is correlated with the contact stiffness k_n and k_s as,

$$k_n = {}^{E(w_C)}\!/_{2} \tag{9}$$

$$k_s = G(w_C) \tag{10}$$

where E is the Young's modulus and G is the shear modulus of the particle assemblage in the absence of a parallel bond. The contact stiffness thus affects the morphology of the evolving lava dome structure (Eqs. (9), (10)). The contact between adjacent particles exists if the applied shear stress is below the maximum value (F_s^{max}) that is calculated by the Mohr-Coulomb failure criterion and is given as,

$$F_s^{max} = C + \mu F_n \tag{11}$$

where C is the material cohesion and coefficient of friction is μ, and F_n is normal contact force given in Eq. (11). Material cohesion is an important parameter and affects the lava dome morphology. Cohesion is represented by bond strength/rigidity of the linear contact bond in the model (Delenne et al., 2004; Guo and Morgan, 2006; Itasca Consulting Group, 2004). Maximum normal (σ_{max}) and shear strength (τ_{max}) for failure of the bond is given as,

$$\sigma_{max} = {}^{P}\!/_{A} \tag{12}$$

$$\tau_{max} = {}^{|v|}\!/_{A} \tag{13}$$

where the macroscopic response of a linear contact bond can be related to that of an elastic beam of area A, subject to pure axial (P) and pure shear loading ($|v|$) given by Eqs. (12), (13). The linear contact bond breaks when the pure axial or shear stress exceeds the material strength.

The values of the macroscopic magnitudes of cohesion and coefficient of friction that we select are based on back-analyses of failure on slopes. The range for cohesion and friction angles obtained from such analyses vary from 0 to 1.1 MPa and 0–45°, which covers the rheologic range of viscous andesite magma through solidified lava (Simmons et al., 2005). It represents the approximate ranges of material strength for major dome collapse events at Soufriere Hills Volcano, during slow to moderate extrusion rates. Idealized material properties of the core and talus considered in our simulation runs are given in Table 3.

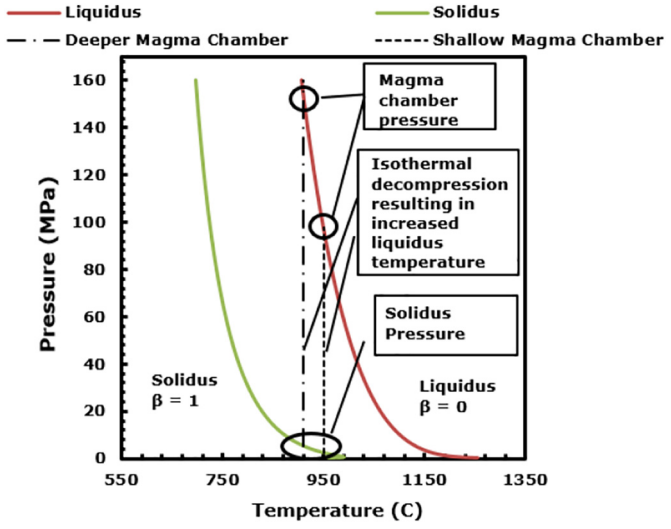

Fig. 3. Phase behavior of magma with variation in pressure and temperature obtained using Eq. (6) for an experimental sample at 160 MPa and 875 °C (initial pressure and temperature) with composition similar to the dome lava obtained at Soufrière Hills Volcano, Montserrat (β indicates crystal content in the material) (Couch et al., 2003; Melnik and Sparks, 2005; Husain et al., 2014).

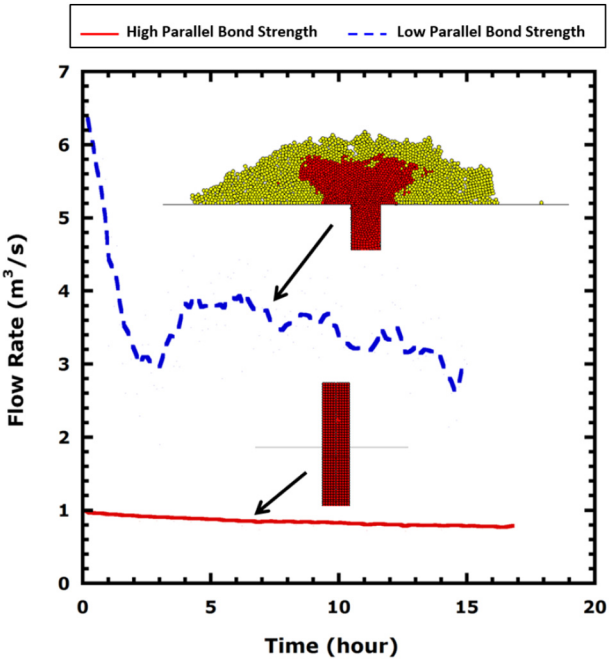

Fig. 4. Flow-rate history assumed to model evolution of simulated lava dome for different parallel bond strengths ($\tau_{max} = 4 \times 10^5$ Pa for low parallel bond strength magma and $\tau_{max} = 4 \times 10^7$ Pa for high parallel bond strength magma). Endogenous dome growth is observed at higher flow rates ($Q \approx 1.5$ to 7 m^3/s) for magma with low parallel bond strength (4×10^5 Pa), while viscous plug flow results at lower flow rates ($Q < 1$ m^3/s) and higher parallel bond strength ($\tau_{max} = 4 \times 10^7$ Pa).

Table 3
Input parameters for model runs to obtain modeled lava dome morphology.

Parameter	Value	
	Talus	Core
Density (kg/m3)	2500	2500
Solidus pressure (MPa)	0.4	–
Particle radius (m)	1.5	1.5
Friction angle	42°	–
Young's Modulus (talus without parallel bond (GPa)	3	0.3

2.1. Apparent viscosity and its effect on dome morphology

An approximation commonly used to describe the non-Newtonian behavior of magma flow is the Bingham flow law where shear stress (τ) is given by,

$$\tau = \tau_0 + \eta\dot{\gamma} \tag{14}$$

where the Bingham yield stress is represented by τ_0 and η is the constant plastic viscosity for a strain rate of $\dot{\gamma}$. Flow initiates on application of a stress greater than the yield strength (τ_0) given by Eq. (14). For small strains, the apparent viscosity (η_{app}) (Eq. (15)) is much higher than the actual viscosity of the fluid and is given by,

$$\eta_{app} = \eta + \frac{\tau_0}{\dot{\gamma}} \tag{15}$$

with both strain rate ($\dot{\gamma}$) and yield stress (τ_0) affecting apparent viscosity (η_{app}). The simulations incorporate Bingham yield strength (τ_0) using τ_{max}, which represents the parallel bond strength in the model and is calculated using Eq. (3). Constant plastic viscosity (η) is correlated to the parallel bond shear stiffness (k^s) in the simulations (Eq. (5)).

The onset of non-Newtonian behavior is observed for a crystal fraction higher than 0.4 and a yield stress $>2 \times 10^6$ Pa (Caricchi et al., 2007; Griffiths, 2000; Lejeune and Richet, 1995). Experimental results indicate that magmas reach a large limiting apparent viscosity caused by the onset of a yield stress for crystal bearing magmas that result in the transition of the magma rheology from Newtonian to Bingham flow with increasing strain rates (Caricchi et al., 2007). Simulation runs (Fig. 4) performed at intermediate flow rates ($Q \approx 1.5$ to 7 m^3/s) and low magma viscosity ($\eta < 1010$ Pa), illustrate that the modeled lava dome evolves endogenously. Strain rates observed in the simulated lava dome during endogenous growth ($Q \approx 1.5$ to 7 m^3/s) range between 10^{-7} to 10^{-3} s^{-1} (Figs. 4 & 5). Similar apparent viscosities were observed in the experiments performed by Pinkerton and Stevenson (1992) for the range of strain rates observed in our simulations (performed with magma of similar composition and range of crystal concentration). The non-Newtonian behavior of magma is enhanced with an increase in crystal fraction at higher strain rates ($\dot{\gamma} > 10{-}3\ s{-}1$) (Fig. 5). The strain rate ($\dot{\gamma}$) is calculated in the model at every time step for each particle (using in-built feature in PFC2D – details in Itasca Consulting Group, 2004). In the subsequent section we further investigate the influence of magma yield strength on the morphology of the lava dome.

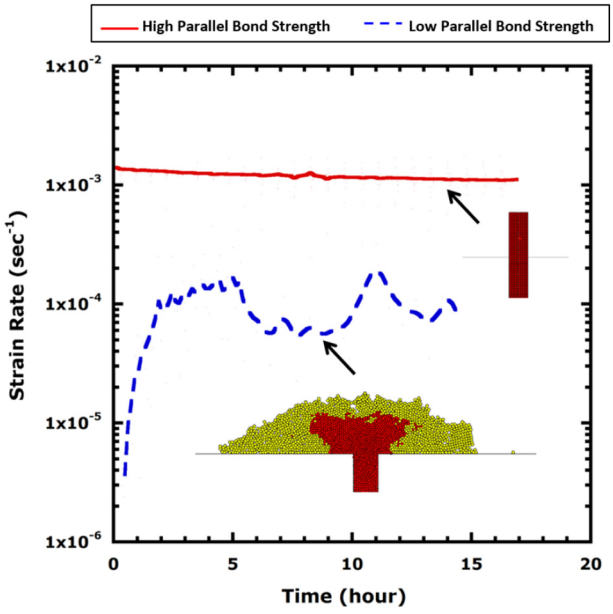

Fig. 5. Strain rates generated during the evolution of the simulated lava dome for the flow-rate history given by Fig. 4. Strain rate values during endogenous growth (low parallel bond strength $\tau_{max} = 4 \times 10^5$ Pa) ranged between 10^{-6} to 10^{-3} s^{-1}, while higher strain rates ($\dot{\gamma} > 10^{-3}$ s^{-1}) are observed during the growth of the upheaved plug with greater parallel bond strength ($\tau_{max} = 4 \times 10^7$ Pa).

3. Results and discussion

Our particle-mechanics model simulations track both temporal and spatial evolution of idealized endogenous lava dome growth. We explore the sensitivity of the patterns of lava dome growth to key adjustable parameters of the mechanical model, and show how the strength properties and extrusion rates influence the morphology of the evolving dome. In Section 3.1, we calibrate magma yield strength (parallel bond strength) against an analytical model (Blake, 1990) and discuss the impact of different parallel bond strengths on the simulated lava dome morphology (endogenous *vs* exogenous). This calibration enables parallel bond strength to be defined, that is then used in the further forward-simulations of Sections 3.2 and 4. In Section 3.2, we extend the forward numerical simulations to generate synthetic lava domes that evolve endogenously. The resulting dome morphologies are compared with those derived both from the analytical model (Blake, 1990) and from independent laboratory observations of analogue experiments, satisfactory agreement is obtained. Finally, in Section 4 we forward-model the lava dome growth observed at SHV, Montserrat, with particular focus on the dome growth period of October 1996 during which the dome evolved endogenously.

3.1. Lava dome flow behavior

The effective bulk viscosity of the magma (mixture of melt and crystal) at any point can be characterized by an apparent flow viscosity that

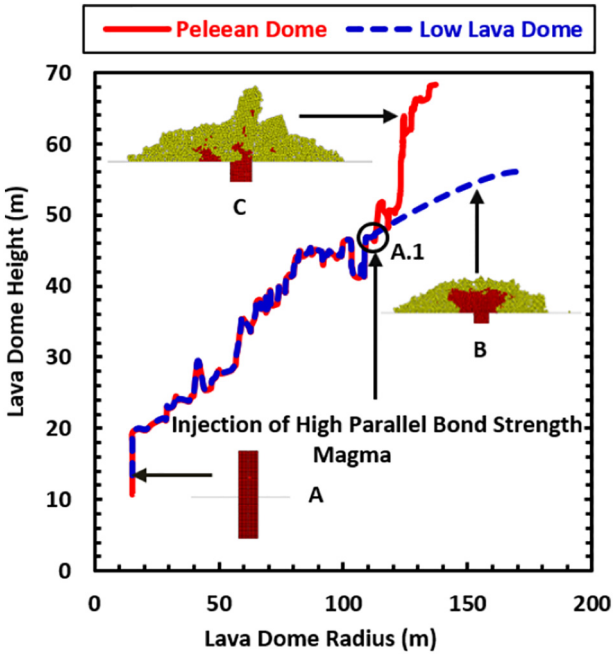

Fig. 6. Evolution of two simulated lava domes with same flow-rate history. The parallel bond strength assigned to the particles of the 2 lava domes is approximately the same ($\tau_{max} = 0.4$ MPa) until the of injection of high parallel bond strength magma (point A.1). An upheaved plug grows initially unobstructed and collapses at the vent (point A). The parallel bond strength of centrally injected magma for the Peleean lava dome is increased (τ_{max} from 0.4 to 40 MPa) at a radius ~ 105 m. The low lava dome continues to grow endogenously (point B), while the Peleean dome grows steeper (point C).

captures the macrophysics of the flow (Eq. (15)), and is a function of the magma yield strength.

Fig. 6 represents our modeled evolution of two lava domes with lava of different parallel bond strength. The variation in apparent bulk yield strength (τ_{0_a}) for the lava dome is calculated from Eq. (16) (Blake, 1990) as

$$\tau_{0_a} = (0.323 \pm 0.016)\left(H^2 \rho g / R_{3D}\right) \quad (16)$$

where H and R_{3D} are the lava dome height and radius for a magma of density ρ and gravitational acceleration g. The previously calculated strength (Eq. (16)) is influenced by the bulk behavior of the dome. In our notation, "apparent bulk yield strength" (τ_{0_a}) is the shear strength calculated using Eq. (16) that is representative of the bulk (macroscale) strength of the rock mass. Conversely, "yield strength" refers to the parallel bond strength (τ_{max}) that is assigned between particles (packets of magma) in the model that is an (microscale) artifact which delivers the bulk yield strength at the macroscale.

Our modeled lava dome evolution is followed as a function of height and radius in Fig. 6 (labeled points A – C) and represents two simulations. Initially the yield strength (represented by the parallel bond strength) is maintained the same for both cases until point A.1 is reached (parallel bond strength (τ_{max}) = 4×10^5 Pa). The yield strength (τ_{max}) is maintained constant throughout the simulation period for the synthetic lava dome represented by the "low" lava dome (low H/R ratio; dashed blue curve in Fig. 6), while the yield strength (τ_{max}) is increased during growth of the other simulated lava dome (from 4×10^5 to 4×10^7 Pa → red curve in Fig. 6). When the dome radius reaches 105 m (labeled point A.1 in Figs. 6 and 7), magma with a higher yield strength (parallel bond yield strength (τ_{max}) = 4×10^7 Pa) is injected into the lava dome core. By implementing the step-change increase in parallel bond strength, we investigate the effect of yield strength on magma rheology and the subsequent flow pattern, which transitions from endogenous to exogenous growth styles.

A solid lava plug (red curve in Fig. 6, point A) develops as the lava extrudes vertically above the vertical conduit, and as no dome yet exists, no further resistance occurs from overlying material (Fig. 6). The drop in the apparent bulk yield strength (τ_{0_a}) in the initial growth phase of the simulated lava dome indicates the point of collapse of the rigid plug (Fig. 7). The extruded plug collapses, spreads out to form a non-spiny lava dome (*i.e.* one that has a low H/R ratio) till point A.1 is reached (Fig. 6). The evolution of the apparent bulk yield strength (τ_{0_a}) for the 2 simulated lava domes is given in Fig. 7. The apparent bulk yield strength of the small lava dome remains approximately constant with time (τ_{0_a} varies between 1.2×10^5 to 1.5×10^5 Pa). The growth of a Pelean dome initiates with the upheaval of a plug with a radius equal to the vent, caused by the injection of the higher parallel bond strength magma (point A.1, where τ_{max} is raised to from 0.4 to 40 MPa). This increases the apparent bulk yield strength (τ_{0_a}) of the lava dome, represented by point A.1 in Fig. 7. This transition in the lava dome morphology is similar to that previously observed (see Blake (1990) Fig. 17a). The behavior is represented in our simulations using variation in parallel bond strength (τ_{max}) which is a proxy for the bulk yield strength of rock mass. It implies that the morphology of the lava dome is principally controlled by the bulk yield strength (τ_0) of the injected magma. The apparent bulk yield strengths estimated for Pelean domes is typically $>10^5$–10^6 Pa (Blake, 1990), while the small lava dome evolves at apparent bulk yield strengths $<10^6$ Pa (Fig. 8). The values of apparent bulk yield strength (τ_{0_a}~0.1 MPa) estimated by Blake, 1990 are slightly different from the parallel bond strength (τ_{max} = 0.4 MPa) used to model low-aspect ratio lava domes, while they are markedly different for Pelean domes (τ_{0_a}~0.28 MPa *vs* τ_{max} = 40 MPa). This behavior is an artifact of the imprint of the dimension from the pre-existing low lava dome on which the Pelean lava dome develops in our simulation model. It highlights a limitation in the analytical model proposed by Blake, 1990 which can be overcome by our numerical simulations.

The small lava domes are defined by a model of spreading Newtonian fluid if the viscous stress in the flowing dome is much greater than the bulk yield strength of the lava. This ratio, termed the Bingham number (B), defines the flow behavior of the fluid (Balmforth and Craster, 2000; Blake, 1990; Griffiths, 2000) and is given as

$$B = \frac{\tau_{0_a}}{\eta\dot{\gamma}} \quad (17)$$

where η is the apparent flow viscosity of the magma for an apparent bulk yield strength of τ_{0_a} at a strain rate of $\dot{\gamma}$. The magnitude of the

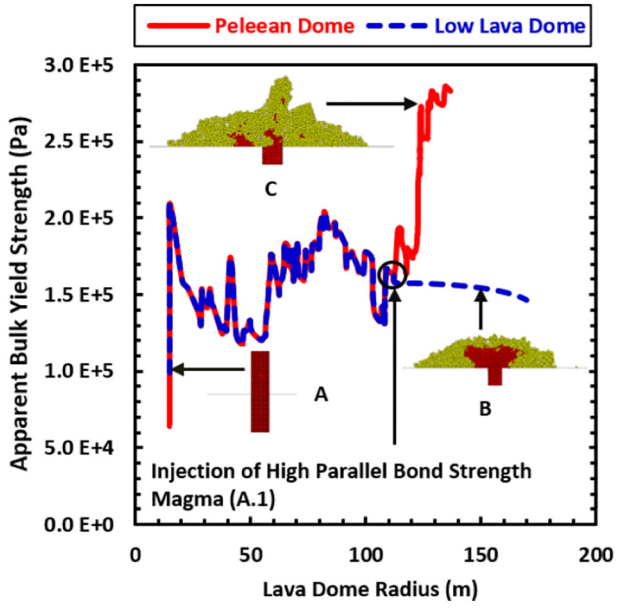

Fig. 7. Variation in apparent bulk yield strength of the simulated lava dome calculated using Eq. (16) and given in Fig. 6. Snapshots of evolving lava dome morphology are taken at points labeled from A–C and shown in Fig. 6.

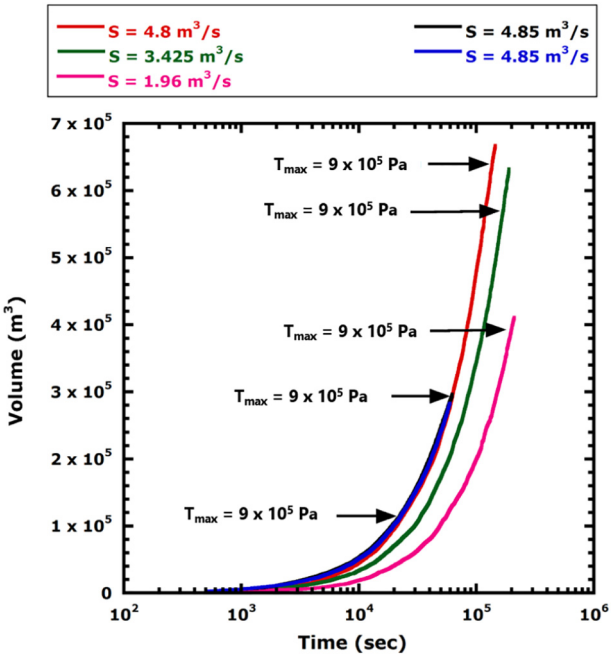

Fig. 8. Volume trend for the modeled lava dome with different parallel bond strength and injection rates which govern the value of S that are expressed by Eq. (19).

viscous stress, $\eta\dot{\gamma}$ in Eq. (17), is much larger than the apparent bulk yield strength (τ_{0_a}) (apparent bulk yield strength = 10^4–10^6 Pa) of the flowing magma for low lava domes ($B \ll 1$). The parametric analyses in the subsequent section explores the evolution of simulated small endogenous lava domes, growing at constant or specified flow-rate history. The simulation results are compared against the analytical model of a spreading viscoplastic lava dome (Blake, 1990) below.

3.2. Analysis of lava dome evolution

In general the magma in lava domes does *not* behave as a Newtonian fluid and may be approximated as a temperature-dependent Bingham material with a bulk yield stress (τ_0) (Blake, 1990; Buisson and Merle, 2002). Comparison of model results assuming purely viscous fluid with highly silicic and extremely viscous (dacite) lavas are unsatisfactory (Griffiths and Fink, 1997). The eruption style and lava dome heights and ratios H/R are consistent with models in which growth is controlled by apparent yield strength (Blake, 1990) or the strength and constraints of an external lava crust (Iverson, 1990).

In the previous section, we illustrated that for a simulated lava dome evolving endogenously, the apparent yield strength (τ_{0_a}) is in good agreement with the parallel bond strength (τ_{max}). Here we compare the growth of the simulated endogenous lava dome with the analytical expression for height of a lava dome evolving due to the injection of magma with a given parallel bond strength (values are approximately equal to apparent yield strength) at a specified volumetric rate. We initially illustrate that the rate of growth of lava dome height for the 2D numerical and 3D analytical model is in good agreement for a specified volume (for parallel bond strength (τ_{max}) ranging between 0.2 and 0.9 MPa) and then obtain an expression for the equivalent 3D radius for the 2D model. The simulation time for the 2D model runs is significantly faster (≈1000 times) in comparison to 3D models, which allow us to investigate a wider range of the parameter space.

Our modeled lava domes are simulated in 2D, and comparison with observed field values requires a 3D model. The development of a 3D model, however, is currently restricted by the very high simulation time required to perform the calculations (this will decrease in future, but current codes are not parallelized). The maximum time step in our model is constrained by the stable mechanical time step ($t = \sqrt{\frac{m_p}{k_n}}$, m_p = mass of particle and k_n = normal contact bond stiffness) and the number of particles in the simulation. The time step in the simulation is increased by considering the particle as a disk with thickness equal to the characteristic width (w_c) (Itasca Consulting Group, 2004). The maximum time step in our simulation run is ~0.5 s and the computational time increases non-linearly with inclusion of additional particles. Thus, a correlation of the 2D model radius with the 3D radius from Blake's (1990) analytical model is obtained and discussed in the later part of the section and in the Appendix A.

Surface cooling can affect carapace strength and influence gross behavior of some domes (Iverson, 1990). The transition of flow from Newtonian to non-Newtonian behavior occurs at time $t^{'}$ and is given by Eq. (18) (Blake, 1990),

$$t^{'(\alpha-5)} = \frac{\tau_{0_a}^8}{g^3\rho^3\eta^5 S} \tag{18}$$

$$V_{3D} = St^{\alpha} \tag{19}$$

noting that S and α are supply rate constants defining total erupted volume (V_{3D}) at time t (Eq. (19)) (Blake, 1990; Huppert et al., 1982). If $\alpha = 1$, volumetric growth is linear with time; growth rate wanes with time for $\alpha < 1$, and waxes with $\alpha > 1$. Shear rates are large near the conduit exit, thus viscous stresses are more important during the early growth period of the lava dome due to a smaller radius to height ratio. A transition occurs from viscous flow ($B \ll 1$) to plastic flow at large times. The value of the Bingham number increases with the strength of the lava, which is controlled by degassing induced crystallization and is a function of effusion rate. Thus, the lava dome growth rate is a function of the yield strength and volumetric recharge rate (Griffiths, 2000). An important implication of Eq. (18) for $\alpha < 5$, is that the initial flow behavior is Newtonian until time $t^{'}$ and then transitions to plastic flow, which then dominates the spreading dynamics of the fluid (Blake, 1990).

Constant flow-rate analog dome-building experiments using kaolin slurry or polyethylene glycol (Blake, 1990; Griffiths and Fink, 1997) define expressions correlating lava dome height and radius for a material with a specified bulk yield strength. The increase in height (H) and radius (R_{3D}) of a Bingham dome are given as a function of time (Blake, 1990; Griffiths, 2000)

$$H = 1.4\left(\tau_{0_a}/\rho g\right)^{2/5} S^{1/5} t^{\alpha/5} \tag{20}$$

$$R_{3D} = 0.65\, S^{2/5}\left(\rho g/\tau_{0_a}\right)^{1/5} t^{2\alpha/5} \tag{21}$$

where all parameters are as previously defined. For a dome growing at a constant effusion rate ($\alpha = 1$), dome growth (height and radius) approaches the trend predicted by Eqs. (20) and (21) after the transition time ($t^{'}$) given by Eq. (18) is exceeded. The transition time ($t^{'}$) (from flow controlled by viscous stress to flow controlled by parallel bond strength) in all simulations (see Figs. 9 and 10) is below ~0.23 days. Blake (1990) found that a simple parabolic curve is a satisfactory model of dome shape and can be integrated to yield an expression of volume as a function of height and radius (see also Appendix A for correlation of R_{2D} with R_{3D})

$$V_{3D} = 8\pi H R_{3D}^2/15 \tag{22}$$

where H and R_{3D} are the height and radius of the evolving dome in the experiment. Fig. 8 represents the volume of our simulated lava dome (with specified S and α values). In Fig. 9 the parallel bond strength (τ_{max})for all simulation runs shown is maintained at constant value of 0.9 MPa, while the efflux rate (S) is varied as 4.8, 3.425 and 1.96 m^3/s.

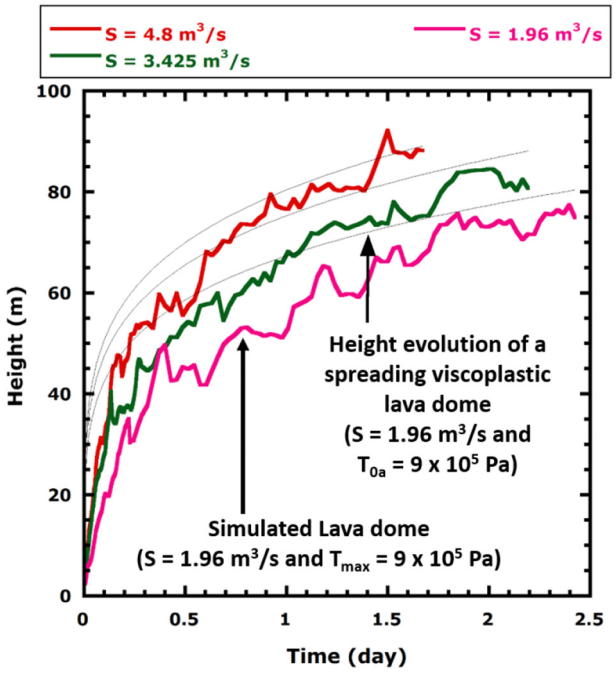

Fig. 9. Evolution of height of the modeled lava dome with constant parallel bond strength (τ_{max} = 0.9 MPa) and different flow rates for which the volume evolution is given in Fig. 8. Simulated height is compared against the analytical solution of a spreading viscoplastic lava dome ((Blake, 1990)) shown in light gray traces.

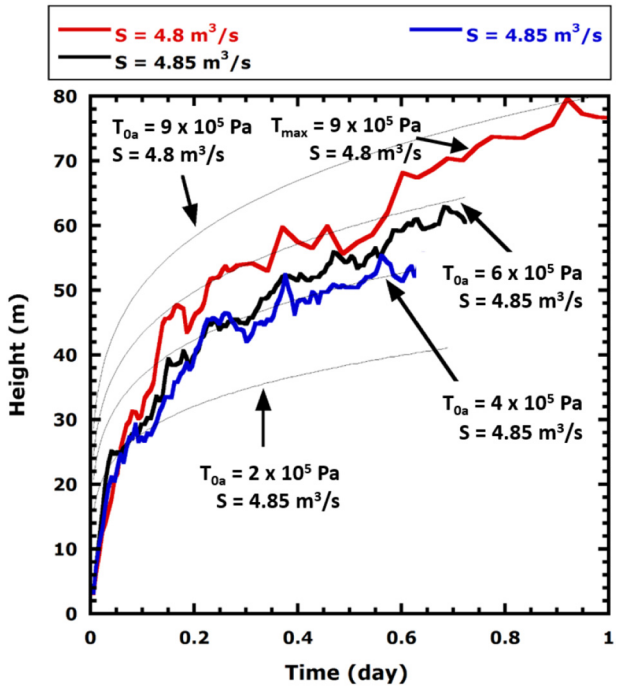

Fig. 10. Evolution of height of the modeled lava dome with constant flow rate and variable parallel bond strength (τ_{max} varies from 0.9 to 0.2 MPa). Simulated height is compared against the analytical solution of a spreading viscoplastic lava dome ((Blake, 1990)) shown in light gray traces.

For these recharge rates, the height of the simulated lava dome evolves as predicted for a Bingham plastic in Eq. (20) (Blake, 1990) (since the transition time is small, the trends agree at short times). The dome height grows at a lower rate (until time $t < 0.75$ days) than the height growth predicted for the constant apparent bulk yield strength case (Eq. (20)). This behavior is similar to observations made by Blake, 1990 in his experiments and was attributed by him to adjustments in the value of S and α when the reservoir was expanding, and to the influence of the finite-size outlet (vent). In our simulations, this effect appears to be the result of higher shear stresses at a lower R/H ratio that diminish as the radius of the simulated lava dome increases. In the Blake (1990) experiments the effect became unimportant by the time $R = 3r$, where R = radius of the dome and r = radius of the vent. We observe that the height of the simulated lava dome with a higher flow rate ($S = 4.8$ m^3/s) approaches the predicted trend earlier, since time is required for the dome radius to grow to 3 times vent radius. Our simulated lava dome height agrees with the analytical models for a constant flux rate ($S = 4.85$ m^3/s), with prescribed apparent bulk yield strengths varying as 0.2, 0.6 and 0.9 MPa. The effect of the constricting force applied on the ductile core by the surrounding talus is more evident in the simulated lava dome with magma of lower parallel bond strength (τ_{max}). The evolution of height for the synthetic lava dome with parallel bond strength of 0.2 MPa matches the analytical trend for height of a lava dome with apparent bulk yield strength of 0.4 MPa (Fig. 10). Thus, for magma with lower apparent bulk yield strength the analytical model fails to capture the effect of the frictional resistance offered by the talus to the spreading of the ductile core.

The simulation runs are in 2D with the geometry shown in Fig. 11. The development of radius in the 2D model is constricted perpendicular to the 2D cross-section of the simulated lava dome. This is observed in Fig. 11. Thus, the radius of the simulated lava dome in 2D grows at a faster rate than in 3D. Figs. 9 and 10 show that the height of the simulated lava domes is equal to the representative 3D value of a spreading viscoplastic material. Assuming that the volume for the simulated lava dome is represented by the parabolic curve given for the viscoplastic analytical model (Eq. (22)), the effective 3D radius is calculated using Eq. (23) from the modeled 2D value and is given as (see Appendix A for detailed discussion)

$$R_{3D} = 3.75\sqrt{R_{2D}} \tag{23}$$

$$R_{3D} = 3.852\,R_{2D}^{0.5165} \tag{24}$$

where R_{3D} is the effective 3D radius calculated from the modeled 2D value represented by R_{2D}. Fig. 12 illustrates the data match of the effective 3D radius, calculated using Eq. (23), with the viscoplastic model based on Eq. (21). Eq. (24) is obtained from a multivariate regression of the simulation data (volume, radius and height) (see Appendix A), showing very close agreement with Eq. (23). The radius (equivalent 3D value) of the simulated lava dome is higher than the predicted viscoplastic analytical value prior to 0.66 days (as simulated lava

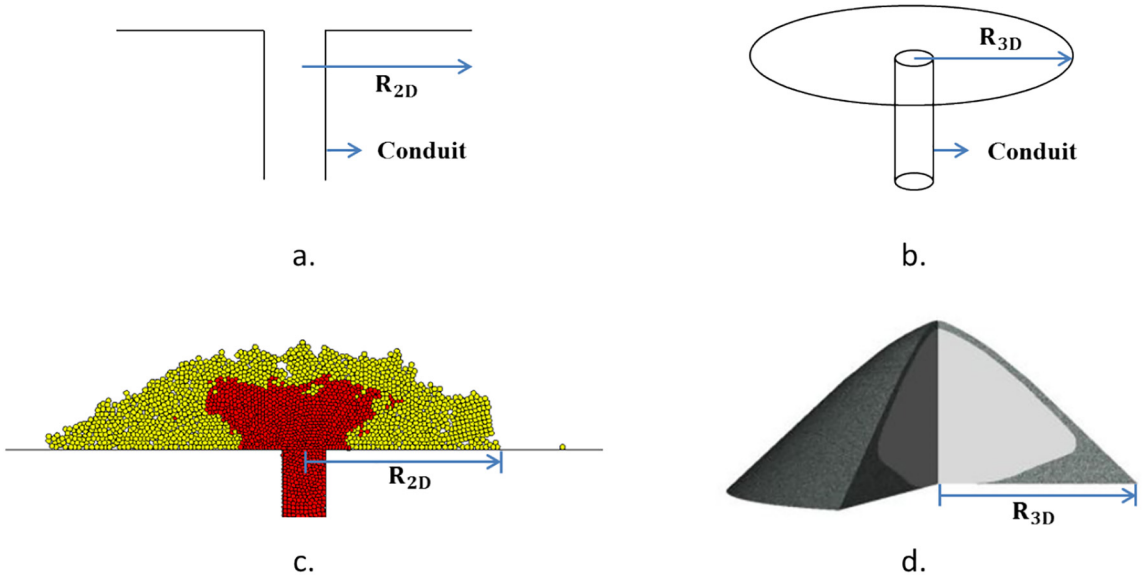

Fig. 11. a) Basic model setup in PFC^{2D} which includes the conduit with a rigid horizontal base b) Basic model setup of an axi-symmetrical model which includes the conduit with a rigid circular horizontal base of radius R_{3D} c) Diagrammatic illustration of the simulated lava dome structure in PFC^{2D} with an elongation of $2R_{2D}$. The spread of the simulated lava dome is aided by the restricted spread along the width. d) Simulated lava dome structure with a radius R_{3D} in an axi-symmetric model (Hale, 2008).

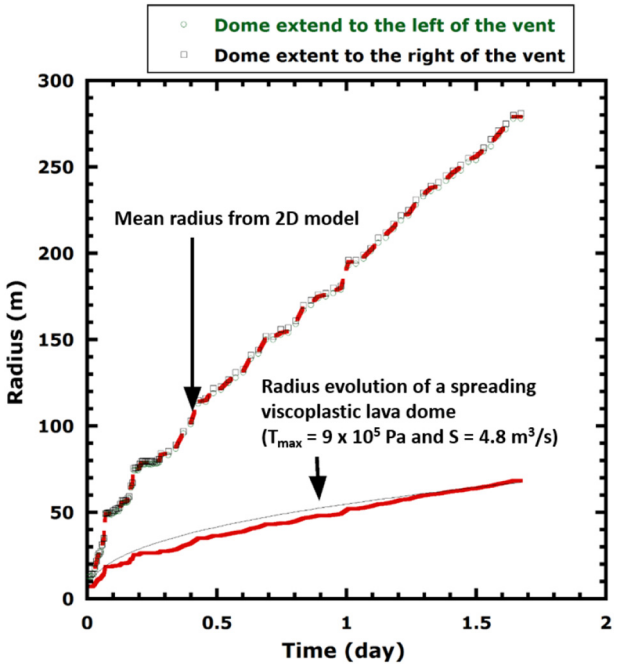

Fig. 12. Evolution of radius of the modeled lava dome. The averaged 2D radius is represented by the red dash line. The representative 3D radius is calculated using Eq. (23) and is illustrates in the figure. The effective 3D radius is compared against the value obtained from the analytical solution of a spreading viscoplastic lava dome for a volume trend match given by S = 4.8 m^3/s ((Blake, 1990)). (For interpretation of the references to color in this figure legend, the reader is referred to the web version of this article.)

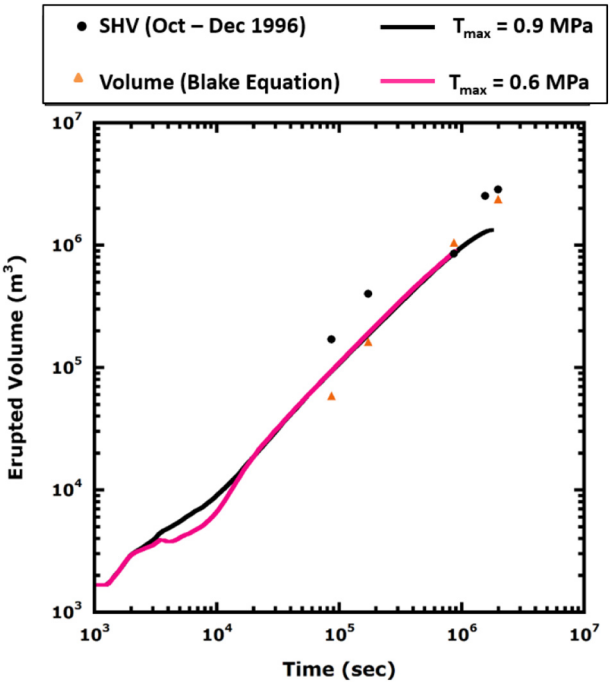

Fig. 13. Trend for the lava dome growth at SHV, Montserrat from October. Simulated volumetric trend follows the best fit time dependent flow-rate function given by Eq. (25). Simulation runs are performed for lava dome with parallel bond strength of 0.6 (23 days of eruption) and 0.9 MPa (54 days of eruption).

dome radius is <3 times the vent radius), but approaches and follows the viscoplastic analytical value for times exceeding 0.66 days.

4. Qualitative observations of dome morphology on Soufriere hills volcano, Montserrat

In this section we compare observations of lava dome growth at SHV with our simulations, and focus particularly on the lava dome growth period from 1st October to 12th December 1996. This was stage IV of the SHV eruption (Watts et al., 2002), with extrusion resuming two weeks after the large 17 September explosive eruption that reamed out the conduit to a depth of (at least) 4 km with the upper part of the conduit widened from substantial expulsion of ballistic ejecta (Robertson et al., 1998). Lava extrusion began on 1st October with initial discharge rate of 1.8 m^3/s (Watts et al., 2002). The new dome consisted of a slab of new lava that spread over loose talus, initially with a smooth surface that evolved to a blocky and spiny appearance typical of the SHV domes (see Figs. 14 and 15 in Watts et al., 2002). Growth continued at a decreased discharge rate and apparently stagnated by 20 October (Watts et al., 2002). On 22nd October extrusion renewed, still at a reduced rate, but was focused only in the central part of the dome where it formed a central raised area (see Fig. 13b Watts et al., 2002). By early November dome growth rates diminished to <1 m^3/s, dome height stagnated at 900 m asl, and strong shallow earthquake swarms began that continued into December, accompanied by the first clear evidence of endogenous activity in the eruption (Watts et al., 2002; Young et al., 2002). This endogenous infilling affected not only the southern parts of the October lobe but also the June 1996 lava in which the 17 September 1996 explosion scar had developed. The zone of swelling was elongate (c. 800 × 300 m) with the main axis aligned east – west, and south of the rim of the explosion scar (see Fig. 2 in Young et al., 2002).

We focus on the lava dome growth rates during this period (1st–23rd October 1996) which varied from 2 to 0.2 m^3/s (Hale and Wadge, 2008). The volumetric increment over the eruptive episode is given in Fig. 13. The flow-rate history assumed in our simulations was selected to represent the observed volumetric increase and the best-fit curve of the time dependent function of flow-rate (Q_{3D}) (Eq. (25)) is given by

$$Q_{3D} = 1.7341 - 0.0274 t'_d \tag{25}$$

where t'_d is time in days and Q_{3D} is in m^3/s. The resulting simulation volumetric increment is shown in Fig. 13. The volumetric flow rate at SHV was observed to decrease from 2.2 m^3/s on 3rd October (on day 3) to 0.7 m^3/s on 7th October (day 7) and ramped up again to 2.4 m^3/s on 14th October (day 14) (Hale and Wadge, 2008). The linear decline best fit curve assumed in the simulation model fails to capture this variation in flow rate and thus results in a cumulative volume of 4.73 Mm^3 as opposed to the observed value of 6.37 Mm^3 (Sparks et al., 1998). Apparent bulk yield strength estimates calculated using Eq. (16) for each pair of height and radius show a substantial variation with time. Apparent bulk yield strength increases with time from 0.1 MPa (on 1 day of this period) to 0.9 MPa (on 54 day). The calculated apparent bulk yield strength values are estimates based on the lava dome height and radius (Eq. (16)). The dome grew endogenously and unconstrained in the earlier collapse scar, during the first 3 weeks (up until 22nd October 1996). The lateral spread of the lava dome at the end of initial 3 weeks of growth was then constrained by the earlier dome remnants. The dome continued to grow centrally, thus the height increased, while the radial spread was constricted, leading to subsequent growth that is largely exogenous (Hale and Wadge, 2008). Thus, the apparent bulk yield strength estimates obtained using Eq. (18) increased from ~0.6 MPa (22nd October 1996) to 0.9 MPa (23rd November 1996). Our simulations focus on representing the endogenous growth phase at SHV, Montserrat which lasted for ~23 days (22nd October 1996).

Fig. 14 represents the evolution of the simulated lava dome height. The results are compared against the lava dome at SHV, Montserrat. Fig. 14 shows the dome height at 23 days after this dome growth phase initiated. After 5 days the simulated lava dome height approaches

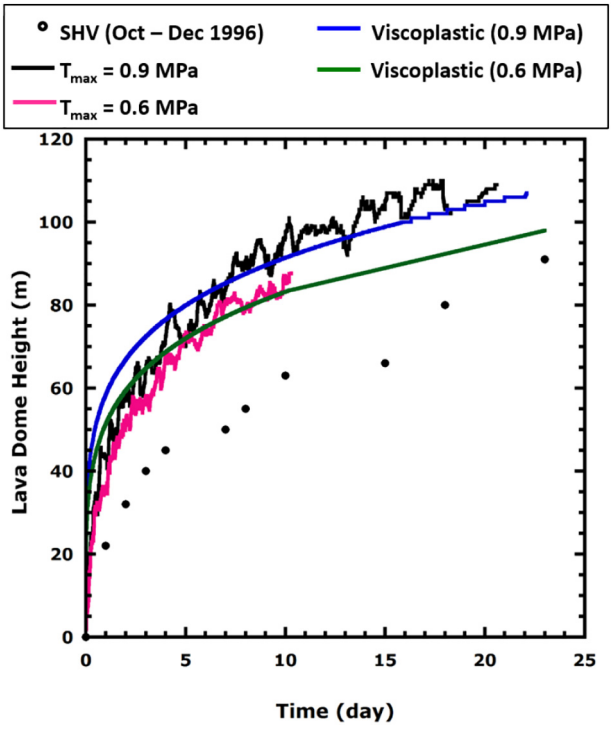

Fig. 14. Observed evolution of height of the lava dome growth at SHV, Montserrat from October 1996. Height predicted by the analytical solution (green and blue curve) for lava dome with parallel bond strength of 0.6 MPa is 98 m and the observed height at 23 days is 91 m. Simulated lava dome height (cyan and black curve) follows the analytical trend (blue and green curve) after time exceeds 5 days. (For interpretation of the references to color in this figure legend, the reader is referred to the web version of this article.)

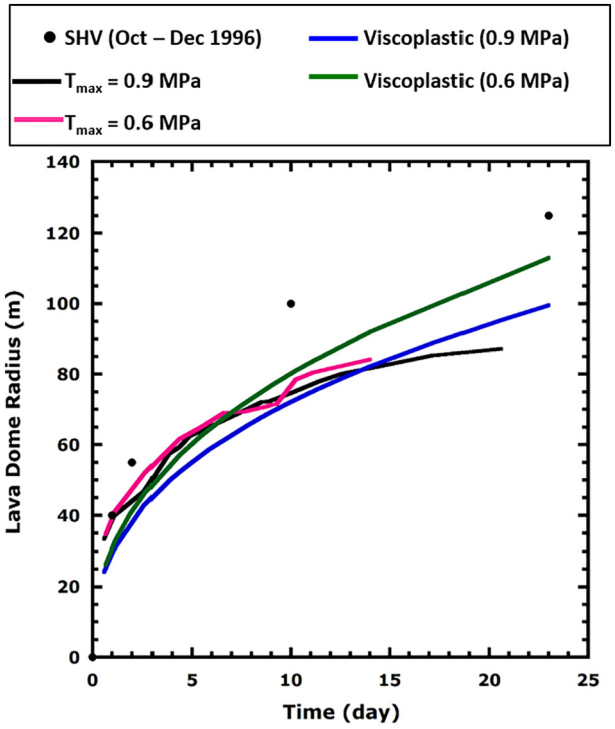

Fig. 15. Observed evolution of radius of the lava dome growth at SHV, Montserrat from October1996. Analogous 3D radius (cyan and black curve) and analytical trend (blue and green curve) predicted follows a trend given by $R \alpha t^{0.2857}$ that is slightly lower than the observed trend (mean radius calculated from the lava dome volume) given by $R \alpha t^{0.3643}$. (For interpretation of the references to color in this figure legend, the reader is referred to the web version of this article.)

and then follows the predicted analytical trend (assumed parallel bond strength and apparent bulk yield strength of 0.6 and 0.894 MPa) for a spreading viscoplastic dome. The height predicted for the lava dome with an apparent bulk yield strength of 0.6 MPa at the end of 23 days in close agreement with the height (91 m) observed at SHV, while the simulated height (107 m) is higher for an apparent bulk yield strength of 0.9 MPa. The calculated apparent flow viscosity for the lava dome with apparent bulk yield strength of 0.6 and 0.894 MPa is approximately 1.36×10^{11} and 2.6×10^{11} Pa·s respectively (Table 4 for the parameters used in the calculation). The apparent viscosity at moderate strain rates (10^{-2} to 10^{-5} s^{-1}) for crystal rich andesitic and rhyolitic lava is in the range of 10^{9} to 10^{12} Pa·s (Lavallée et al., 2007). The calculated apparent flow viscosities are in the range of final viscosity values assumed in the study by Hale (2008) to simulate the lava dome growth (Newtonian fluid core with a deformable talus) (10^{10} to 10^{12} Pa·s) at SHV.

The evolution of radii for our simulated lava domes are shown in Fig. 15, with the effective 3D radius calculated using Eq. (24). For times earlier than 5 days, the effective 3D radius is higher than the value calculated with Eq. (21), where apparent bulk yield strengths are 0.6 and 0.894 MPa. The increased radius compensates for the lower value of height during this period of the simulation. The effective 3D radius evolves at a slightly lower rate ($R \alpha t^{0.2857}$) compared to the observed radius growth rate ($R \alpha t^{0.3643}$) at SHV, as the volume calculated using Eq. (25) fails to capture the nuances in field value (fluctuations in magma flow rate) and slightly under-predicts lava dome volume. The predicted volume trend ($V \alpha R^{3.4805}$) is in close agreement with the best fit to the observed trend ($V \alpha R^{3.25}$). The reduced radial spread at later times (≥5 days) is possibly due to the effect of the frictional resistance of the talus on the evolving dome and the slightly under-predicted value of the simulated volume from the observed trend (Table 5).

At intermediate extrusion rates (1.5–7 m^3/s) the SHV lava dome growth is endogenous. The modeled endogenous lava dome consists of a cohesive core and frictional carapace. A simulation with low apparent bulk yield strength (parallel bond strength 10^4 to 10^6 Pa) results in endogenous growth with the evolution of a small lava dome (with low H/R ratio) (Figs. 8, 9, 11, 12 and 14). The range of material apparent bulk yield strengths (parallel bond strengths) for the core is in agreement with the values obtained in the study performed for the spreading of a viscoplastic lava dome (Blake, 1990). The morphology of the evolving lava domes differs significantly and are governed by the flow-rate history and parallel bond strength.

Table 4
Value of constants used in the calculation of apparent flow viscosity for the lava dome evolution at SHV, Montserrat during the period from 1 to 20 October 1996. The constants (S and α) are the best fit obtained to the height of the simulated lava dome and thus differ for magma with different yield strength as the values.

Bulk yield strength value (MPa)	Constant	
	S	*A*
0.894	1.4786	0.9662
0.6	0.7118	1.0277

5. Conclusion

Magma ascent rates and decompression paths largely control the evolution of magma properties and contribute to the evolving morphology of complex lava domes. We present a model that incorporates evolving strength and rheology (spatially) into a growing volcanic pile. Our model provides a first-order understanding of the effects of apparent bulk yield strength on simulated lava dome morphology, building on analytical work by Huppert et al. (1982) and Blake (1990). Dome morphology is sensitive to yield strength, a small change in this parameter exerts a large influence on the pattern of dome growth.

Table 5
Notation.

Symbol	Description	Unit
v_{3D}^{avg}	Average fluid velocity given by Hagen – Poisseuille's flow equation	LT^{-1}
Q_{3D}	Flow rate in 3D geometry	$L^3\,T^{-1}$
a_{3D}	Area of conduit for a 3D geometry	L^2
v_{3D}	Flow velocity of fluid for 3D geometry	LT^{-1}
r	Radius of conduit	L
F_n	Normal force applied on the particle in contact with another in PFC^{2D}	MLT^{-2}
k_n	Normal contact bond stiffness	MT^{-2}
δ_n	Overlap in the normal direction between 2 contacting particle in PFC^{2D}	L
F_s	Shear force applied on the contacting particle in PFC^{2D}	MLT^{-2}
k_s	Shear contact bond stiffness	MT^{-2}
δ_s	Particle overlap in the shear direction in PFC^{2D}	L
C	Material cohesion	$ML^{-1}\,T^{-2}$
μ	Coefficient of friction of the material	–
σ_{max}	Tensile strength of the material	$ML^{-1}\,T^{-2}$
ΔL	Change in length on application of normal force on the sample/particle	L
L_o	Original length of the sample/particle	L
D	Original diameter of the sample/particle	L
E	Young's modulus	–
G	Shear modulus	–
Δx	Change in length of the sample/particle in the shear direction	L
η	Fluid viscosity	$ML^{-1}\,T^{-1}$
k^n, k^s	Parallel bond normal and shear stiffness respectively	$ML^{-2}\,T^{-2}$
ΔU^s	Shear displacement for a given time step Δt	L
V_i	Shear velocity for the given time step Δt	LT^{-1}
w_C	Characteristic width of the conduit to represent the 3D flow rate to its representative value for the 2D geometry	L
Φ	Friction angle of the material	–
A	Area on which force is applied	L^2
A_o	Area of sample/particle before deformation	L^2
τ_{max}	Shear strength of the material	$ML^{-1}\,T^{-2}$
$\lvert v \rvert$	Numerical value of pure shear force applied	MLT^{-2}
$T_{liq,\,sol}$	Temperature of the magma in the solution state	–
$T_{solidus}$	Temperature of the magma below which the magma solidifies for a given pressure	–
p	External pressure acting on the magma during the eruption cycle	$ML^{-1}\,T^{-2}$
a_T	Constant for the empirical expression to obtain the phase behavior of the magma at Soufrière Hills Volcano, Montserrat	–
b_T	Constant for the empirical expression to obtain the phase behavior of the magma at Soufrière Hills Volcano, Montserrat	–
c_T	Constant for the empirical expression to obtain the phase behavior of the magma at Soufrière Hills Volcano, Montserrat	–
d_T	Constant for the empirical expression to obtain the phase behavior of the magma at Soufrière Hills Volcano, Montserrat	–
V_{2D}	Erupted volume in the 2D model	$L^3\,T^{-1}$
V_{3D}	Erupted volume in 3D	$L^3\,T^{-1}$
R_{2D}	Radius of the simulated lava dome in the 2D model	L
R_{3D}	Radius of the lava dome in 3D	L
h	Height of the simulated lava dome in 2D model	L
H	Height of the lava dome in 3D	L
τ_o	Bulk yield strength	$ML^{-1}\,T^{-2}$
τ_{0_a}	Apparent bulk yield strength	$ML^{-1}\,T^{-2}$
B	Bingham number	–
$\dot{\gamma}$	Strain Rate	T^{-1}
S	Constant to match the volume trend given by Eq. (19)	$L^3\,T^{-1}$
α	Constant to match the volume trend given by Eq. (19)	–
P	Pure axial loading	$M^1L^1T^{-2}$
t'	Time taken for flow behavior to transition from Newtonian to non-Newtonian	T^1
t'_d	Time in days	T^1
v	Pure shear loading	$M^1L^1T^{-2}$

Transition from low aspect ratio lava domes (*i.e.* those in which the apparent bulk yield strength of the magma is in the range of 10^4–10^6 Pa) extruded at intermediate flow rates ($Q \approx 1.5$ to 7 m^3/s), to Pelean domes (*i.e.* those in which the apparent bulk yield strength of the lava is $>10^5$–10^6 Pa) extruded at lower flow rates ($Q < 1$ m^3/s), occurs when degassing-induced crystallization has markedly increased the strength of the material.

Our simulations are intended to improve understanding of dome growth patterns such as observed at SHV and in particular the effect of yield strength on lava dome morphology. Degassing-induced crystallization, as observed at SHV, causes increased strength. The evolution of magma strength causes the viscous material, comprising the core of the lava dome, to become stiffer, which we model here by increasing the parallel bond strength between adjacent particles. The increase in yield strength in turn produces a transition of rheology, resulting in the development of a Pelean lava dome with spine growth (Bingham flow with high yield strength and low flow rate), from an initial dome of lower height that had grown endogenously (dominantly viscous flow, with low yield strength, and higher flow rate). Simulation results discussed in Section 3.1 (Figs. 6 and 7) represent this transition in the lava-dome morphology, resulting from the increased yield strength of the injected magma.

In addition, we conclude that yield strength plays a dominant role during dome growth even where surface cooling from radiation is not significant (Griffiths & Fink, 1993). The height and eruptive style of highly silicic and extremely viscous lava extrusion is consistent with analytical models where growth is controlled by the yield strength of the magma (Blake, 1990). The simulation results discussed in Section 3.2 are tested against a theoretical solution for a spreading viscoplastic lava dome (Blake, 1990) that is well-constrained by scaled laboratory

experiments. Our new numerical simulations exhibit a good agreement with Blake's analytical models for times that exceed the flow transition time calculated using Eq. (18).

For crystal-bearing magmas such as those erupted at SHV, the magma evolves toward large apparent viscosities which influence magma rheology and growth style (Caricchi et al., 2007). We have focused our numerical simulations in Section 4 on dome growth observed at SHV during October 1996. Our simulated lava dome height for parallel bond strength of 0.6 MPa follows the theoretical solution, which is in more or less close agreement to the observed height. The apparent flow viscosity (~1.36×10^{11} Pa·s for apparent bulk yield strength of 0.6 MPa) calculated from the simulation result is in the range of estimated viscosities (10^9 to 10^{12} Pa·s) for andesitic-dacitic composition crystal rich lavas (Hale, 2008; Lavallée et al., 2007). Improved estimates of yield strength of lava dome core material should enhance the fidelity of numerical simulations to actual dome growth eruptions.

Acknowledgement

This work is a partial result of support from the NASA_ROSES program (26-1201-2661), which is gratefully acknowledged. Valuable experience with volcanic domes on Montserrat was obtained by BV, DE and GM with the support of several grants from the US National Science Foundation, and for BV also by the British Government. Several anonymous reviewers examined our paper, and one in particular reviewed it several times. We appreciate their insights and perseverance, and our paper is better because of it.

Appendix A

I. Correlation of normal stiffness (k_n) with Young's Modulus

Force–Displacement equation is given by Eq. (A.1) as

$$F_n = -k_n \delta_n \tag{A.1}$$

Young's modulus and deformation are related by Eq. (A.2)

$$F_n = -{EA_o \Delta L}/{L_o} \tag{A.2}$$

Area perpendicular to the applied force is given by Eq. (A.3)

$$A_o = D.(w_C) \tag{A.3}$$

Thus, stiffness is given by Eq. (A.4)

$$k_n = {ED(w_C)}/{L_o} \tag{A.4}$$

Original length of sample is obtained and is given by Eq. (A.5)

$$L_o = D \tag{A.5}$$

Therefore, stiffness is given Eq. (A.6)

$$k_n = E(w_C) \tag{A.6}$$

II. Correlation of Shear stiffness (k_n) with Shear Modulus

The Force-Displacement equation is given by Eq. (A.7)

$$F_s = -k_s \delta_s \tag{A.7}$$

The expression for shear modulus is given by Eq. (A.8)

$$F_s = -{GA\Delta x}/{L_o} \tag{A.8}$$

Hence the correlation between shear stiffness and shear modulus is given by Eq. (A.9)

$$k_s = G(w_C) \tag{A.9}$$

III. Correlation of 2D flow rate with actual 3D values

Average velocity of a fluid flowing through a pipe can be expressed by Hagen – Poisseuille's flow and is given by Eq. (A.10)

$$v_{3D} = {Q_{3D}}/{a_{3D}} \tag{A.10}$$

If the flow velocity in the 2D model (specified in the simulation run) is maintained equal to the 3D value, then to correlate the flow rate in the 2 cases, an equivalent characteristic length/width is calculated. Characteristic length is the width of the 2D model (which for most models is considered as unit thickness). The correlation is given by Eqs. (A.11) and (A.12)

$$\pi r^2 = L\,(w_C) \tag{A.11}$$

$$w_C = {\pi r^2}/{L} \tag{A.12}$$

IV. Correlation of microscopic modulus for particle-particle contact with contact stiffness

Using Eq. (A.6), the microscopic modulus of a particle-particle contact bond (in the absence of a parallel bond) is given by Eq. (A.13)

$$E_c = k_n(w_C) \tag{A.13}$$

V. Correlation of microscopic modulus for parallel bond with parallel bond stiffness

Parallel bond stiffness is expressed in units of stiffness per unit area and is given by Eq. (A.14)

$$k^n = {E_p}/{L_0} \tag{A.14}$$

The original length of the particle system is expressed in Eq. (15). The microscopic modulus for parallel bond is given by Eq. (A.15)

$$E_p = k^n D \tag{A.15}$$

VI. Correlation of radius in 2D model with an effective 3D value

Total volume of the simulated lava dome of radius (R_{2D}) and thickness (w_c) in the 2D model is given by Eq. (A.16)

$$V_{2D} = R_{2D}\, h\, w_c \tag{A.16}$$

Integral of the simple parabolic curve is observed to fit the experimental data of the volume of the slurry dome obtained by Blake (1990) and is given by Eq. (A.17)

$$V_{3D} = 8\pi H R_{3D}^2/15 \tag{A.17}$$

Assuming the volume in both the lava domes (3D and 2D geometry) is equal (same flow-rate history). Equating Eqs. (A.16) and (A.17) to obtain Eq. (18)

$$R_{2D}\, h\, w_c = 8\pi H R_{3D}^2/15 \tag{A.18}$$

The evolution of height of the simulated lava dome (2D model) is observed to be in agreement with the predicted values obtained from the analytical solution. Thus, the radius in the 2D model is correlated with the 3D radius in Eq. (A.19) as

$$R_{3D} = 3.75\sqrt{R_{2D}} \tag{A.19}$$

The best-fit curve obtained by the multivariable regression analysis (coefficient of determination – $R^2 = 0.9854$) for the simulation data is given by Eq. (A.20)

$$V_{2D} = R_{2D}\, h\, w_c \tag{A.21}$$

VII. Correlation of Parallel Bond Stiffness with Viscosity

The ductile core material is treated as a non-Newtonian fluid (Bingham fluid). The material flow initiates on the application of stress greater than the material yield stress (τ_{max}). The correlation of constant plastic viscosity with applied stress (τ) is given by

$$\Delta\tau = \tau - \tau_{max} = -\eta\frac{\partial V}{\partial y} \tag{A.22}$$

If the change in shear stress ($\Delta\tau$) is positive, then flow initiates and is affected by the parallel bond shear stiffness. Change in shear force for a given time step (Δt) on the particle due to parallel bond shear stiffness is given by Eq. (A.23)

$$\Delta F^s = -k^s A \Delta U^s \tag{A.23}$$

Change in shear displacement for a given time step in PFC^{2D} is given by Eq. (A.24)

$$\Delta U^s = V_i \Delta t \tag{A.24}$$

Change in shear stress due to parallel bond shear stiffness is given by Eq. (A.25)

$$\Delta\tau = -k^s V_i \Delta t \tag{A.25}$$

Equating Eqs. (A.22) and (A.25) to give Eq. (A.26)

$$-k^s V_i \Delta t = -\eta\frac{\partial V}{\partial y} \tag{A.26}$$

Dividing both sides by the same length (y) results in Eq. (A.27)

$$-k^s \Delta t\, y\frac{V_i}{y} = -\eta\frac{\partial V}{\partial y} \tag{A.27}$$

In Eq. (51), the term $\frac{V_i}{y}$ and $\frac{dV}{dy}$ is the shear velocity per unit length of the material/fluid. Thus viscosity is related to parallel bond shear stiffness by Eq. (A.28)

$$\eta = k^s \Delta t y \tag{A.28}$$

Hence parallel bond stiffness acts as the plastic viscosity term in the modeling of the bonded material. The effective plastic viscosity in the model is influenced by the time step magnitude which is a function of the mass of the particle and the linear contact stiffness. Thus a change in the size of the time step affects the plastic viscosity of the modeled particle assemblage.

References

de' Michieli Vitturi, M., Clarke, A.B., Neri, A., Voight, B., 2008. Effects of conduit geometry on magma ascent dynamics in dome-forming eruptions. Earth Planet. Sci. Lett. 272, 567–578. https://doi.org/10.1016/j.epsl.2008.05.025.

Allen, M.P., Tildesley, D.J., 1989. Computer Simulation of Liquids. Science Publications, Oxford.

Balmforth, N.J., Craster, R.V., 2000. Dynamics of cooling domes of viscoplastic fluid. J. Fluid Mech. 422, 225–248.

Barclay, J., Rutherford, M.J., Carroll, M.R., Murphy, M.D., Devine, J.D., Gardner, J., Sparks, R.S.J., 1998. Experimental phase equilibria constraints on pre-eruptive storage conditions of the Soufriere Hills magma. Geophys. Res. Lett. 25, 3437–3440. https://doi.org/10.1029/98GL00856.

Blake, S., 1990. Viscoplastic models of lava domes. In: Fink, J. (Ed.), Lava Flows and Domes SE - 5, IAVCEI Proceedings in Volcanology. Springer, Berlin Heidelberg, pp. 88–126 https://doi.org/10.1007/978-3-642-74379-5_5.

Blundy, J., Cashman, K., 2001. Ascent-driven crystallisation of dacite magmas at Mount St Helens, 1980–1986. Contrib. Mineral. Petrol. 140, 631–650. https://doi.org/10.1007/s004100000219.

Blundy, J., Cashman, K., Humphreys, M., 2006. Magma heating by decompression-driven crystallization beneath andesite volcanoes. Nature 443, 76–80.

Bourgouin, L., Mühlhaus, H.-B., Jane Hale, A., Arsac, A., 2007. Studying the influence of a solid shell on lava dome growth and evolution using the level set method. Geophys. J. Int. 170, 1431–1438. https://doi.org/10.1111/j.1365-246X.2007.03471.x.

Buisson, C., Merle, O., 2002. Experiments on internal strain in lava dome cross sections. Bull. Volcanol. 64, 363–371. https://doi.org/10.1007/s00445-002-0213-6.

Caricchi, L., Burlini, L., Ulmer, P., Gerya, T., Vassalli, M., Papale, P., 2007. Non-Newtonian rheology of crystal-bearing magmas and implications for magma ascent dynamics. Earth Planet. Sci. Lett. 264, 402–419. https://doi.org/10.1016/j.epsl.2007.09.032.

Cashman, K., Blundy, J., 2000. Degassing and crystallization of ascending andesite and dacite. Philos. Trans. R. Soc. Lond. Ser. A 358, 1487–1513. https://doi.org/10.1098/rsta.2000.0600.

Couch, S., Harford, C.L., Sparks, R.S.J., Carroll, M.R., 2003. Experimental constraints on the conditions of formation of highly calcic plagioclase microlites at the Soufrire Hills Volcano, Montserrat. J. Petrol. 44, 1455–1475. https://doi.org/10.1093/petrology/44.8.1455.

Cundall, P.A., Strack, O.D.L., 1979. A discrete numerical model for granular assemblies. Geotechnique 29, 47–65.

Delenne, J.-Y., El Youssoufi, M.S., Cherblanc, F., Bénet, J.-C., 2004. Mechanical behaviour and failure of cohesive granular materials. Int. J. Numer. Anal. Methods Geomech. 28, 1577–1594. https://doi.org/10.1002/nag.401.

Denlinger, R.P., 1990. A model for dome eruptions at Mount St. Helens, Washington based on subcritical crack growth. In: Fink, J. (Ed.), Lava Flows and Domes SE - 4, IAVCEI Proceedings in Volcanology. Springer, Berlin Heidelberg, pp. 70–87 https://doi.org/10.1007/978-3-642-74379-5_4.

Fink, J.H., Griffiths, R.W., 1990. Radial spreading of viscous-gravity currents with solidifying crust. J. Fluid Mech. 221, 485–509.

Griffiths, R.W., 2000. The dynamics of lava flows. Annu. Rev. Fluid Mech. 32, 477–518. https://doi.org/10.1146/annurev.fluid.32.1.477.

Griffiths, R.W., Fink, J.H., 1993. Effects of surface cooling on the spreading of lava flows and domes. J. Fluid Mech. 252, 667–702.

Griffiths, R.W., Fink, J.H., 1997. Solidifying Bingham extrusions: a model for the growth of silicic lava domes. J. Fluid Mech. 347, 13–36.

Guo, Y., Morgan, J.K., 2006. The frictional and micromechanical effects of grain comminution in fault gouge from distinct element simulations. J. Geophys. Res. Solid Earth 111, B12406. https://doi.org/10.1029/2005JB004049.

Hale, A.J., 2008. Lava dome growth and evolution with an independently deformable talus. Geophys. J. Int. 174, 391–417. https://doi.org/10.1111/j.1365-246X.2008.03806.x.

Hale, A.J., Wadge, G., 2003. Numerical modelling of the growth dynamics of a simple silicic lava dome. Geophys. Res. Lett. 30, 2003. https://doi.org/10.1029/2003GL018182.

Hale, A.J., Wadge, G., 2008. The transition from endogenous to exogenous growth of lava domes with the development of shear bands. J. Volcanol. Geotherm. Res. 171, 237–257. https://doi.org/10.1016/j.jvolgeores.2007.12.016.

Hammer, J.E., Rutherford, M.J., 2002. An experimental study of the kinetics of decompression-induced crystallization in silicic melt. J. Geophys. Res. Solid Earth 107, ECV 8-1–ECV 8-24. https://doi.org/10.1029/2001JB000281.

Hort, M., 1998. Abrupt change in magma liquidus temperature because of volatile loss or magma mixing: effects on nucleation, crystal growth and thermal history of the magma. J. Petrol. 39, 1063–1076. https://doi.org/10.1093/petroj/39.5.1063.

Huppert, H.E., Shepherd, J.B., Haraldur Sigurdsson, R., Sparks, S.J., 1982. On lava dome growth, with application to the 1979 lava extrusion of the soufrière of St. Vincent. J. Volcanol. Geotherm. Res. 14, 199–222. https://doi.org/10.1016/0377-0273(82)90062-2.

Husain, T., Elsworth, D., Voight, B., Mattioli, G., Jansma, P., 2013. Influence of infusion rate and magma rheology on the growth of lava domes. 47th US Rock Mechanics/Geomechanics Symposium 2013.

Husain, T., Elsworth, D., Voight, B., Mattioli, G., Jansma, P., 2014. Influence of extrusion rate and magma rheology on the growth of lava domes: Insights from particle-dynamics modeling. J. Volcanol. Geotherm. Res. 285, 100–117. https://doi.org/10.1016/j.jvolgeores.2014.08.013.

Husain, T., Elsworth, D., Voight, B., Mattioli, G., Jansma, P., 2018. Influence of conduit flow mechanics on magma rheology and the growth style of lava domes. Geophys. J. Int. 213, 1768–1784. https://doi.org/10.1093/gji/ggy073.

Innocenti, S., Andreastuti, S., Furman, T., del Marmol, M.-A., Voight, B., 2013a. The pre-eruption conditions for explosive eruptions at Merapi volcano as revealed by crystal texture and mineralogy. J. Volcanol. Geotherm. Res. 261, 69–86. https://doi.org/10.1016/j.jvolgeores.2012.12.028.

Innocenti, S., del Marmol, M.-A., Voight, B., Andreastuti, S., Furman, T., 2013b. Textural and mineral chemistry constraints on evolution of Merapi Volcano, Indonesia. J. Volcanol. Geotherm. Res. 261, 20–37. https://doi.org/10.1016/j.jvolgeores.2013.01.006.

Itasca Consulting Group, 2004. PFC2D User's Guide. Itasca Consulting Group, Inc.

Iverson, R.M., 1990. Lava domes modeled as brittle shells that enclose pressurized magma, with application to Mount St. Helens. In: Fink, J. (Ed.), Lava Flows and Domes SE - 3, IAVCEI Proceedings in Volcanology. Springer, Berlin Heidelberg, pp. 47–69 https://doi.org/10.1007/978-3-642-74379-5_3.

Lavallée, Y., Hess, K.-U., Cordonnier, B., Bruce Dingwell, D., 2007. Non-Newtonian rheological law for highly crystalline dome lavas. Geology 35, 843–846. https://doi.org/10.1130/G23594A.1.

Lejeune, A.-M., Richet, P., 1995. Rheology of crystal-bearing silicate melts: an experimental study at high viscosities. J. Geophys. Res. Solid Earth 100, 4215–4229. https://doi.org/10.1029/94JB02985.

Marsh, B., 1989. MAGMA PHYSICS magma physics. Geophysics SE - 85, Encyclopedia of Earth Science. Springer, US, pp. 676–688 https://doi.org/10.1007/0-387-30752-4_85.

Matuttis, H.-G., Chen, J., 2014. Understanding the Discrete Element Method: Simulation of Non-Spherical Particles for Granular and Multi-body Systems. John Wiley & Sons Inc.

Melnik, O., 2000. Dynamics of two-phase conduit flow of high-viscosity gas-saturated magma: large variations of sustained explosive eruption intensity. Bull. Volcanol. 62, 153–170. https://doi.org/10.1007/s004450000072.

Melnik, O., Sparks, R.S.J., 2002. Modelling of conduit flow dynamics during explosive activity at Soufrière Hills Volcano, Montserrat. Geol. Soc. Lond. Mem. 21, 307–317. https://doi.org/10.1144/GSL.MEM.2002.21.01.14.

Melnik, O., Sparks, R.S.J., 2005. Controls on conduit magma flow dynamics during lava dome building eruptions. J. Geophys. Res. Solid Earth 110, B02209. https://doi.org/10.1029/2004JB003183.

Morgan, J.K., McGovern, P.J., 2005a. Discrete element simulations of gravitational volcanic deformation: 2. Mechanical analysis. J. Geophys. Res. Solid Earth 110, B05403. https://doi.org/10.1029/2004JB003253.

Morgan, J.K., McGovern, P.J., 2005b. Discrete element simulations of gravitational volcanic deformation: 1. Deformation structures and geometries. J. Geophys. Res. Solid Earth 110, B05402. https://doi.org/10.1029/2004JB003252.

Pinkerton, H., Stevenson, R.J., 1992. Methods of determining the rheological properties of magmas at sub-liquidus temperatures. J. Volcanol. Geotherm. Res. 53, 47–66. https://doi.org/10.1016/0377-0273(92)90073-M.

Robertson, R., Cole, P., Sparks, R.S.J., Harford, C., Lejeune, A.M., McGuire, W.J., Miller, A.D., Murphy, M.D., Norton, G., Stevens, N.F., Young, S.R., 1998. The explosive eruption of Soufriere Hills Volcano, Montserrat, West Indies, 17 September, 1996. Geophys. Res. Lett. 25, 3429–3432. https://doi.org/10.1029/98GL01442.

Rust, A.C., Manga, M., 2002. Effects of bubble deformation on the viscosity of dilute suspensions. J. Non-Newtonian Fluid Mech. 104, 53–63. https://doi.org/10.1016/S0377-0257(02)00013-7.

Rutherford, M.J., Devine, J.D., 2003. Magmatic conditions and magma ascent as indicated by hornblende phase equilibria and reactions in the 1995–2002 Soufrière Hills magma. J. Petrol. 44, 1433–1453. https://doi.org/10.1093/petrology/44.8.1433.

Simmons, J., Elsworth, D., Voight, B., 2005. Classification and idealized limit-equilibrium analyses of dome collapses at Soufrière Hills volcano, Montserrat, during growth of the first lava dome: November 1995–March 1998. J. Volcanol. Geotherm. Res. 139, 241–258. https://doi.org/10.1016/j.jvolgeores.2004.08.009.

Sparks, R.S.J., 1997. Causes and consequences of pressurisation in lava dome eruptions. Earth Planet. Sci. Lett. 150, 177–189. https://doi.org/10.1016/S0012-821X(97)00109-X.

Sparks, R.S.J., et al., 1998. Magma production and growth of the lava dome of the Soufriere Hills volcano, Montserrat: November 1995 to December 1997. Geophys. Res. Lett. 25, 3421–3424.

Sparks, Murphy, Lejeune, Watts, Barclay, Young, 2000. Control on the emplacement of the andesite lava dome of the Soufriere Hills volcano, Montserrat by degassing-induced crystallization. Terra Nova 12, 14–20. https://doi.org/10.1046/j.1365-3121.2000.00267.x.

Stasiuk, M.V., Jaupart, C., 1997. Lava flow shapes and dimensions as reflections of magma system conditions. J. Volcanol. Geotherm. Res. 78, 31–50. https://doi.org/10.1016/S0377-0273(97)00002-4.

Stasiuk, M.V., Jaupart, C., Sparks, R.S.J., 1993. On the variations of flow rate in non-explosive lava eruptions. Earth Planet. Sci. Lett. 114, 505–516. https://doi.org/10.1016/0012-821X(93)90079-O.

Stevenson, D.S., Blake, S., 1998. Modelling the dynamics and thermodynamics of volcanic degassing. Bull. Volcanol. 60, 307–317. https://doi.org/10.1007/s004450050234.

Tallarico, A., Dragoni, M., 2000. A three-dimensional Bingham model for channeled lava flows. J. Geophys. Res. Solid Earth 105, 25969–25980. https://doi.org/10.1029/2000JB900201.

Voight, B., Young, K.D., Hidayat, D., Subandrio, Purbawinata, M.A., Ratdomopurbo, A., Suharna, Panut, Sayudi, D.S., LaHusen, R., Marso, J., Murray, T.L., Dejean, M., Iguchi, M., Ishihara, K., 2000. Deformation and seismic precursors to dome-collapse and fountain-collapse nuées ardentes at Merapi Volcano, Java, Indonesia, 1994–1998. J. Volcanol. Geotherm. Res. 100, 261–287. https://doi.org/10.1016/S0377-0273(00)00140-2.

Voight, B., Komorowski, J.-C., Norton, G.E., Belousov, A.B., Belousova, M., Boudon, G., Francis, P.W., Franz, W., Heinrich, P., Sparks, R.S.J., Young, S.R., 2002. The 26 December (Boxing Day) 1997 sector collapse and debris avalanche at Soufrière Hills Volcano, Montserrat. Geol. Soc. Lond. Mem. 21, 363–407. https://doi.org/10.1144/GSL.MEM.2002.021.01.17.

Watts, R.B., Herd, R.A., Sparks, R.S.J.S.J., Young, S.R., Barmin, A., Melnik, O., Clarke, A.B., Stephens, S., Teasdale, R., Diller, K., Voight, B., Miller, A.D., Stewart, R.C., Hoblitt, R.P., Ewart, J., Aspinall, W.P., Baptie, B., Calder, E.S., Cole, P., Druitt, T.H., Hartford, C., Jackson, P., Lejeune, A.M., Lockhart, A.B., Loughlin, S.C., Luckett, R., Lynch, L., Norton, G.E., Robertson, R., Watson, I.M., Nakada, S., Shimizu, H., Ohta, K., 2002. Growth patterns and emplacement of the andesitic lava dome at Soufrière Hills Volcano, Montserrat. J. Volcanol. Geotherm. Res. 283, 115–152. https://doi.org/10.1126/science.283.5405.1138.

Young, S.R., Voight, B., Barclay, J., Herd, R.A., Komorowski, J.-C., Miller, A.D., Sparks, R.S.J., Stewart, R.C., 2002. Hazard implications of small-scale edifice instability and sector collapse: a case history from Soufrière Hills Volcano, Montserrat. Geol. Soc. Lond. Mem. 21, 349–362. https://doi.org/10.1144/GSL.MEM.2002.021.01.16.